

THE EFFECTS OF ATMOSPHERIC MODELING COVARIANCE ON GROUND-BASED HYPERSPECTRAL MEASUREMENTS OF SURFACE REFLECTANCE

Farid Qamar^{1,2}, Angie S. Gómez-Fonseca³, Gregory Dobler^{2,4,5,6}

¹ Department of Civil and Environmental Engineering, University of Delaware, Newark, DE, USA

² Biden School of Public Policy and Administration, University of Delaware, Newark, DE, USA

³ Department of Physics, National University of Colombia, Bogotá D.C., Colombia

⁴ Department of Physics and Astronomy, University of Delaware, Newark, DE, USA

⁵ Data Science Institute, University of Delaware, Newark, DE, USA

⁶ Center for Urban Science and Progress, New York University, New York, NY, USA

ABSTRACT

This paper presents a novel framework for estimating the covariance and uncertainties of atmospheric parameters and the reflectance spectra of urban surfaces in high-resolution ground-based hyperspectral images. By integrating open source software for atmospheric modeling and statistical sampling, we demonstrate the use of Markov Chain Monte Carlo (MCMC) sampling to quantify the full posterior distributions in a joint fit of both molecular concentrations for atmospheric attenuation and parameterized surface reflectance to spectroscopic observations of an urban scene. We present a use case at visible and near-infrared wavelengths (0.4-1.0 micron) in ~850 spectral channels where the uncertainty in atmospherically corrected surface reflectance of vegetation in the scene is acquired by propagating the uncertainties obtained from modeling the reflectance of a nearby building surface.

Index Terms— Remote Sensing, Hyperspectral, Albedo, Atmospheric Correction, MCMC, Atmospheric Parameter Covariance

1. INTRODUCTION

Hyperspectral imaging (HSI), capable of capturing the intensity for each pixel in an image in hundreds of wavelength channels, has emerged in the past two decades as a precise, non-invasive, and versatile tool used in a variety of domains. In the context of urban science, hyperspectral imaging has been employed for a wide range of applications including the identification of surfaces and materials [1, 2], monitoring the health of vegetation [3, 4, 5], identification of plant species [6, 7], and the detection of atmospheric components and trace gases along the line of sight [8, 9]. While most remote sensing studies utilize hyperspectral imaging from satellite and aerial imaging [10, 11], more recently, ground-based, stationary side-facing observatories [12, 13, 14, 15] have been gaining momentum due to their cost-effectiveness and increased spatial resolution.

In daytime hyperspectral imaging at visible and near-infrared (VNIR) wavelengths of 0.4-1.0 micron, solar radiation interacts with the atmosphere and the imaged foreground object, undergoing significant modifications before it reaches the sensor. A spectrum recorded by ground-based VNIR spectrometers is the product of three main wavelength-dependent components: the incident solar irradiance; the molecular atmospheric attenuation from various gases and water vapor absorption as well as aerosol extinction; and the surface reflectance of the imaged object. The only component of the incident beam on the sensor that is the property of the imaged object

is the surface reflectance. Although it is possible to obtain some information on the imaged surfaces directly from the unedited incident beam spectra, atmospheric effects can significantly influence the quality of extracted information [16, 17]. Hence, disentangling the atmospheric attenuation from the wavelength dependence of the reflectivity, and assessing the associated uncertainties due to covariance between the estimated atmospheric attenuation and surface albedo, is of particular importance for the use of hyperspectral imaging to study properties of the objects in a given scene.

Atmospheric radiative transfer codes are commonly used in remote sensing applications to separate atmospheric effects from the surface's reflectivity [18, 19]. By taking atmospheric parameters (such as water vapor content, atmospheric gases and aerosol concentrations) as inputs, atmospheric transfer codes model the effects of the propagation of light through the atmosphere prior to reaching the sensor. However, due to the challenges of obtaining accurate atmospheric parameters at the precise time the hyperspectral image is captured, assumptions and standard atmospheres are commonly utilized which introduce inaccuracies to the produced models [20]. Therefore, inverse modeling methods for estimating atmospheric parameters and recovering surface reflectivity have become more common [21, 22], though the various atmospheric parameters as well as the surface albedo are known to have some level of covariance [23], motivating inverse modeling studies that explore the complete range of uncertainties (including those covariances) in both atmospheric parameters and surface reflectivity.

Markov Chain Monte Carlo (MCMC) sampling [24, 25] is commonly used for parameter estimation through inverse modelling. Given a likelihood function, rather than identifying the best fit parameters to maximize the likelihood, MCMC samples parameter space based on the acceptance probabilities of the likelihood function to generate full posterior parameter distributions. In this work, we demonstrate the use of MCMC with an atmospheric radiative transfer model to retrieve the atmospheric components and their uncertainties together with the range of possible albedo functions of a building facade in a ground-based, side-facing, hyperspectral image. We then further demonstrate the use of jointly modeling atmospheric attenuation and the building's albedo to retrieve the reflectance spectrum of nearby vegetation.

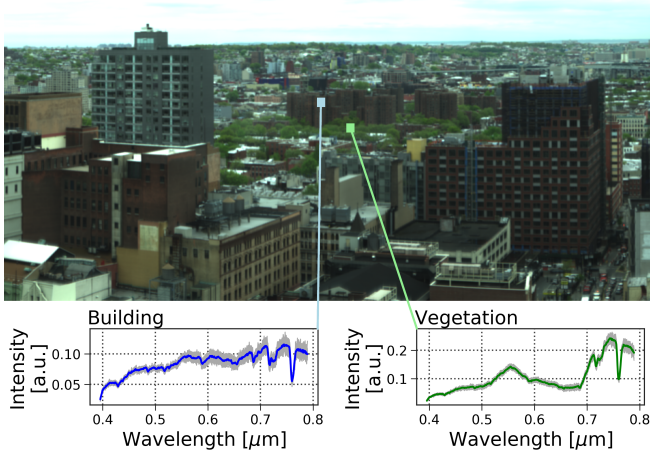


Fig. 1. *Top:* RGB ($0.61\mu\text{m}$, $0.54\mu\text{m}$, and $0.475\mu\text{m}$) representation of the scene imaged by the Urban Observatory’s VNIR hyperspectral imaging system. *Bottom:* Grey lines showing the spectra of 25 (5×5) pixels of a building (*left*) and vegetation (*right*), and their mean spectrum shown in blue and green, respectively.

2. MATERIALS AND METHODS

2.1. Hyperspectral Imaging Data

The hyperspectral imaging (HSI) data used in this work was obtained by the “Urban Observatory” (UO) facility in New York City (NYC) [12, 26, 15]. The UO-deployed VNIR instrument [13, 27] was placed atop a tall ~ 120 m (~ 400 ft) building in Brooklyn with a South-facing horizontally aligned pointing. The instrument is a single slit scanning spectrograph with 1600 vertical pixels sensitive to $0.4\mu\text{m}$ to $1.0\mu\text{m}$ in 848 spectral channels (spectral resolution, FWHM, of 0.72 nm), however, the spectra beyond $0.8\mu\text{m}$ were clipped due to low signal-to-noise ratio at longer wavelengths. A composite RGB image of the scene used in this work is produced by mapping the $0.61\mu\text{m}$, $0.54\mu\text{m}$, and $0.475\mu\text{m}$ channels to the red, green, and blue values respectively is shown in Fig. 1.

Two sets of pixels were chosen from the scene for this particular work, a 5×5 square of a concrete building surface shown as a blue square, and an adjacent 5×5 square of vegetation shown as a green square in Fig. 1. The range of spectra for both sets of urban materials - human-built and natural - are also presented in Fig. 1 together with their respective mean spectra used in this work for the purpose of atmospheric modelling.

The at-sensor signal of the building and vegetation pixels can be expressed as

$$S_{\lambda}^M = I_{\lambda} \cdot A_{\lambda} \cdot R_{\lambda}^M, \quad (1)$$

where S_{λ}^M is the measured intensity of a material M at wavelength λ , I_{λ} is the solar irradiance, A_{λ} is the atmospheric attenuation, and R_{λ}^M is the material’s reflectance. The particular choice of pixels for the buildings and vegetation in Fig. 1 was to ensure that both the incident top-of-atmosphere solar irradiance and atmospheric attenuation are as similar as possible for the building and vegetation patches, leaving reflectance as the only variable that depends on material type. The reflectance of a concrete surface in VNIR is dominated by the albedo of concrete since its absorption occurs at wavelengths $\sim 10\text{--}13\mu\text{m}$. The albedo of concrete exhibits significant wavelength dependent variations based on a number of factors, in-

cluding porosity, color, water content, and even surface moisture [28, 29]. In this work, we approximate the albedo’s wavelength dependence by a bimodal Gaussian function as seen in eq. 2 that captures its general shape at $\sim 0.4\text{--}0.8\mu\text{m}$,

$$R_{\lambda}^B = \sum_{n=1}^2 b_i e^{-(\lambda - \mu_i)^2 / 2\sigma_i^2} + d. \quad (2)$$

The reflectance spectrum of vegetation, on the other hand, is far more complex. It tends to be dependent on a variety of factors including plant species, development stage, season, leaf position angle and optical properties, and nutrient and stress condition among others [30]. Therefore, by choosing the concrete building pixels to be in close proximity to the vegetation, we extract the reflectance curve of the vegetation and its uncertainty by identifying the atmospheric attenuation component (A_{λ}) through modeling the at-sensor signal of the adjacent concrete building.

2.2. Atmospheric Modeling and MCMC

Several codes exist for modeling atmospheric parameters in remote sensing, however, the majority are known to be computationally demanding [31, 32]. Given that MCMC requires a large sampling pool to converge, we chose the Simple Model for Atmospheric Radiative Transfer of Sunshine (SMARTS2) [33, 34] for this work due to its relative computational efficiency and available range of wavelengths. Using a single core on an Intel Xeon E7 4830 V4 2.00 GHz processor, SMARTS2 has a median runtime of ~ 0.04 seconds to generate an atmospheric model given input concentrations. For the purposes of modeling the building’s at-sensor signal (S_{λ}^B) in eq. (1), the following SMARTS2 parameters were held constant throughout the MCMC sampling:

- The extraterrestrial top-of-atmosphere solar irradiance spectrum I_{λ} was set to the synthesized spectrum from Gueymard, 2004 [35];
- The latitude, longitude, and altitude of the hyperspectral camera’s location in Brooklyn, the height of the building on which it was placed, its tilt angle and surface azimuth, and the day, month, year, and hour of when the hyperspectral image was obtained;
- The concentrations of gases whose absorption coefficients are outside the $0.4\text{--}0.8\mu\text{m}$ range of wavelengths of the image used in this scene (CH_2O , CH_4 , CO , CO_2 , HNO_3 , NO , BrO , ClNO , N_2O , N_2 , NH_3) were set to zero;
- The aerosol model was set to the Shettle and Fenn humidity-dependent urban aerosol model [36].

SMARTS2 produces models that are comparable to those from rigorous radiative codes [34] with calculation time lower by a factor of more than 25 [37]. However, by default SMARTS2 was not built to work with large-scale sampling routines in high-dimensional parameter space. The SMARTS2 Linux implementation is written in Fortran77, whereby it reads user-specified atmospheric parameters and albedo reflectance from ascii files and outputs the computed atmospheric models into separate ascii files. To perform MCMC sampling in this work, we use the Python implementation of the affine-invariant MCMC ensemble sampler, emcee [38]. Therefore, the following modifications to SMARTS2 were required to provide interoperability with the Python statistical ecosystem, including emcee, and the ability to perform quick log-likelihood calculations:

- SMARTS2 Fortran77 code was wrapped using Numpy’s F2py tool [39], making its subroutines callable from Python;

- All functions of SMARTS2 requiring the reading from files that are not fully static were converted to input callable arguments in the main subroutine. This includes all input atmospheric parameters, as well as the reflectance spectra;
- All values for gas concentrations, from natural abundance or pollution, that are either user input, computed, or assumed default values in SMARTS2, were modified to be passed as arguments to the main subroutine by the MCMC sampler;
- The main subroutine was modified to output the relevant final set of calculated wavelengths and spectra to arrays rather than writing results to files.

Without the above modifications to SMARTS2's file I/O functionality, a single model sampling step together with file operations takes on average ~ 3.1 seconds. The above modifications reduced this value to ~ 0.02 seconds, and allowed for the use of parallel computation when sampling the likelihood function. For this sampling, emcee was configured to sample the following variables ($\vec{\theta}$): μ_i , σ_i , b_i ($i = \{1, 2\}$), and d - the parameters for the bimodal Gaussian function for the albedo of concrete in eq. 2; RH [%] - relative humidity at site level; H_2O [g/cm^2] - precipitable water above the site altitude; O_3^{Ab} and O_3^p [$atm-cm$] - ozone total-column abundance above site level and tropospheric ozone due to pollution, respectively; HNO_2 , NO_2 , NO_3 , SO_2 [$atm-cm$] - total-column abundances including tropospheric concentrations of gases with absorption coefficients in the $0.4-0.8\mu m$ wavelength range; and O_2 [$atm-cm$] - total column abundance of oxygen. Uniform priors were used to constrain all parameters into physically meaningful values. For the probability calculation, we use a Gaussian likelihood function,

$$\ln p(y|\lambda, \vec{\theta}, \varepsilon) = -\frac{1}{2} \sum_{\lambda} \left[\frac{(y_{\lambda} - S_{\lambda}(\vec{\theta})^B)^2}{\varepsilon_{\lambda}^2} + \ln(2\pi\varepsilon_{\lambda}^2) \right], \quad (3)$$

where y is the observed mean at-sensor building spectrum shown in Fig. 1 and ε represents an amount by which the noise is underestimated.

3. RESULTS

The posterior distributions of the model parameters for both molecular atmospheric concentrations as well as the building reflectance are shown in Fig. 2. In particular, Fig. 2(a) shows the range and covariances of atmospheric parameters of A_{λ} (eq. 1), while Fig. 2(b) shows the same for the albedo reflectance component of the building spectrum R_{λ}^B . Note, although the figure shows the atmospheric and building parameters as separate corner plots, the likelihood function was sampled across all parameters simultaneously, and we show only these subsections of the full corner plot for space considerations. The contours in the plots represent 1σ , 2σ , and 3σ uncertainties for each parameter, and contours that appear cutoff by the edge of their plot axes are the result of priors limiting the parameters to be ≥ 0 in order to be physically meaningful. The median and 3σ uncertainty for each parameter is shown in Table 1.

Using 3σ samples from this posterior to generate models for A_{λ} and R_{λ}^B , we show each component of eq. 1 as well as the range of model outputs for the observed signal in Fig. 3. The figure demonstrates the range of reflectance spectra of the building's surface given noise in the detector and covariance between albedo and molecular atmospheric concentrations.

By constraining the albedo of the building surface (R_{λ}^B), we are able to isolate the range of potential atmospheric attenuation spectra.

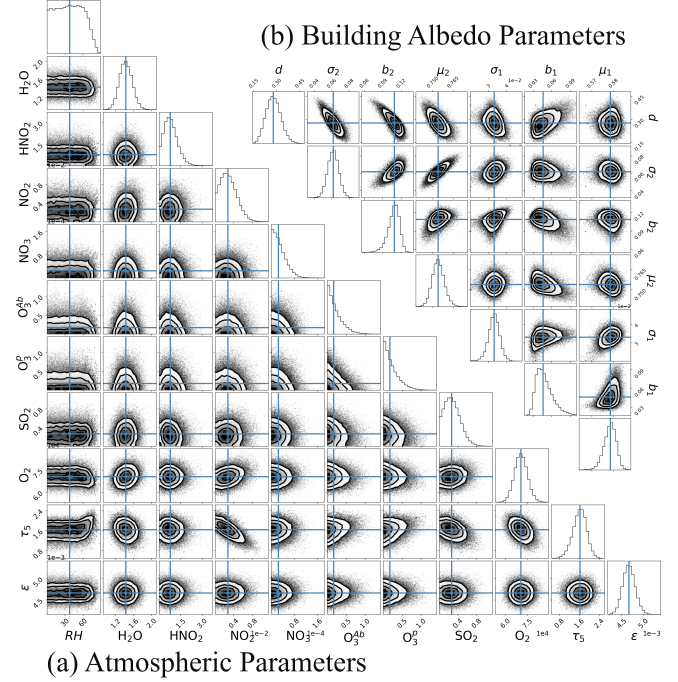


Fig. 2. MCMC results from modelling the at-sensor signal of the building surface with SMARTS2. (a) shows the corner plot of the atmospheric parameters, and (b) shows the corner plot for the albedo parameters in the bimodal Gaussian. Table 1 shows the median value and 3σ uncertainty for all parameters. The full version of this corner plot can be found at: https://cuspuo.org/VNIR_covariance/MCMC_corner.png

Table 1. MCMC median and 3σ uncertainty (including the full parameter covariance derived from the posteriors in Fig. 2) of the albedo and atmospheric parameters obtained from modelling the at-sensor signal of the building surface with SMARTS2. Precipitable water (H_2O) is in units of g/cm^2 , all other gas concentrations are in $atm-cm$.

Parameter	-3σ	Median	$+3\sigma$
μ_1	0.572	0.579	0.583
b_1	0.0293	0.0462	0.0807
σ_1	0.0265	0.0331	0.039
μ_2	0.746	0.754	0.763
b_2	0.0866	0.109	0.123
σ_2	0.0496	0.0618	0.0743
d	0.191	0.277	0.376
RH	1.95	37.7	76.2
H_2O	1.16	1.43	1.72
HNO_2	0.0885	0.772	1.87
NO_2	0.000223	0.00273	0.00676
NO_3	1.11e-06	2.48e-05	8.36e-05
O_3^{Ab}	0.00666	0.169	0.713
O_3^p	0.00665	0.174	0.736
SO_2	0.0202	0.265	0.649
O_2	62300	70500	79400
τ_5	1.06	1.63	2.13
ε	0.0044	0.00466	0.00496

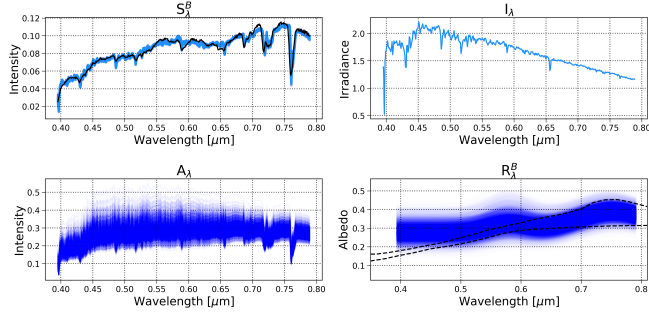


Fig. 3. The components of eq. 1. *Top left:* Range of at-sensor signal models produced by SMARTS2 using MCMC sampling (blue) against the mean at-sensor signal of the building pixels (black) S_{λ}^B . *Top Right:* Extraterrestrial top-of-atmosphere solar irradiance spectrum I_{λ} . *Bottom left:* Range of atmospheric attenuation models produced using the parameters in Fig. 2 A_{λ} . *Bottom right:* Range of uncertainties in albedo curves, (blue) R_{λ}^B , and two of the SMARTS2 template concrete albedo curves (black dashed) for reference.

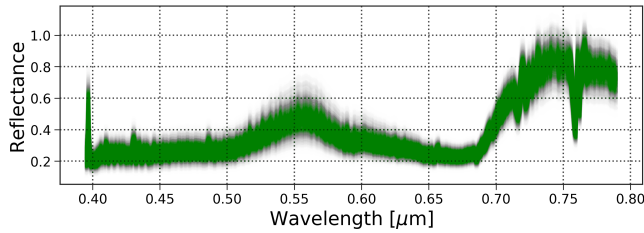


Fig. 4. Range of uncertainty in the atmospherically corrected reflectance spectrum of vegetation (R_{λ}^V), obtained by propagating uncertainties from dividing the mean at-sensor vegetation spectrum (S_{λ}^V) by the solar irradiance spectrum (I_{λ}) and atmospheric attenuation (A_{λ}).

We can then use these (together with the solar irradiance spectrum) to determine the range of reflectance spectra for nearby materials that are affected by the same atmospheric attenuation. For example, we demonstrate this with our spectrum for vegetation in Fig. 4 and note that the upshot of our methodology is that uncertainties and covariances in atmospheric modeling can be propagated into further studies such as vegetative health monitoring.

4. CONCLUSIONS

In this work we have integrated several open source software packages to combine hyperspectral analysis software with statistical sampling. We have developed a framework for estimating the effects of covariance between the absorption of various gas species, scattering, and aerosol extinction in the atmosphere on atmospheric models and the remote measurement of surface reflectances. In particular, we have derived the full posterior distribution for an atmospheric attenuation model at VNIR wavelengths that takes into account the covariances between all atmospheric species as well as parameters of the surface albedo. We have used this framework to demonstrate our ability to propagate uncertainties into corresponding ranges of uncertainty in the reflectance spectra for both human-built and natural surfaces in urban areas. Using these derived uncertainties within context of domain-specific remote sensing studies such as the remote

detection and monitoring of vegetation health, structural integrity in built structures, and gas plume detection and speciation will be the subjects of future work.

5. ACKNOWLEDGEMENTS

This work was supported by a James S. McDonnell Foundation Complex Systems Scholar Award (number:220020434). We thank Gard Groth and Middleton Spectral Vision for their assistance deploying the VNIR camera and data collection.

6. REFERENCES

- [1] Shutao Li, Weiwei Song, Leyuan Fang, Yushi Chen, Pedram Ghamisi, and Jón Atli Benediktsson, “Deep learning for hyperspectral image classification: An overview,” *IEEE Transactions on Geoscience and Remote Sensing*, vol. 57, no. 9, pp. 6690–6709, 2019.
- [2] Farid Qamar and Gregory Dobler, “Pixel-wise classification of high-resolution ground-based urban hyperspectral images with convolutional neural networks,” *Remote Sensing*, vol. 12, no. 16, pp. 2540, 2020.
- [3] E Bauriegel, A Giebel, M Geyer, U Schmidt, and WB Herpich, “Early detection of fusarium infection in wheat using hyper-spectral imaging,” *Computers and Electronics in Agriculture*, vol. 75, no. 2, pp. 304–312, 2011.
- [4] Jan Behmann, Jörg Steinrücken, and Lutz Plümer, “Detection of early plant stress responses in hyperspectral images,” *ISPRS Journal of Photogrammetry and Remote Sensing*, vol. 93, pp. 98–111, 2014.
- [5] Anne-Katrin Mahlein, “Plant disease detection by imaging sensors—parallels and specific demands for precision agriculture and plant phenotyping,” *Plant disease*, vol. 100, no. 2, pp. 241–251, 2016.
- [6] Hiroshi Okamoto, Yumiko Suzuki, and Noboru Noguchi, “Field applications of automated weed control: Asia,” in *Automation: The Future of Weed Control in Cropping Systems*, pp. 189–200. Springer, 2014.
- [7] Charlotte Brabant, Emilien Alvarez-Vanhard, Achour Laribi, Gwénaél Morin, Kim Thanh Nguyen, Alban Thomas, and Thomas Houet, “Comparison of hyperspectral techniques for urban tree diversity classification,” *Remote Sensing*, vol. 11, no. 11, pp. 1269, 2019.
- [8] Rodolphe Marion, Rémi Michel, and Christian Faye, “Measuring trace gases in plumes from hyperspectral remotely sensed data,” *IEEE transactions on geoscience and remote sensing*, vol. 42, no. 4, pp. 854–864, 2004.
- [9] Masoud Ghandehari, Milad Aghamohamadnia, Gregory Dobler, Andreas Karpf, Kerry Buckland, Jun Qian, and Steven Koonin, “Mapping refrigerant gases in the new york city skyline,” *Scientific reports*, vol. 7, no. 1, pp. 1–10, 2017.
- [10] Helmi ZM Shafri, Ebrahim Taherzadeh, Shattri Mansor, and Ravshan Ashurov, “Hyperspectral remote sensing of urban areas: an overview of techniques and applications,” *Research Journal of Applied Sciences, Engineering and Technology*, vol. 4, no. 11, pp. 1557–1565, 2012.

- [11] Muhammad Jaleed Khan, Hamid Saeed Khan, Adeel Yousaf, Khurram Khurshid, and Asad Abbas, "Modern trends in hyperspectral image analysis: a review," *IEEE Access*, vol. 6, pp. 14118–14129, 2018.
- [12] Gregory Dobler, Masoud Ghandehari, Steven E Koonin, Rouzbeh Nazari, Aristides Patrinos, Mohit S Sharma, Arya Tafvizi, Huy T Vo, and Jonathan S Wurtele, "Dynamics of the urban lightscape," *Information Systems*, vol. 54, pp. 115–126, 2015.
- [13] Gregory Dobler, Masoud Ghandehari, Steven E Koonin, and Mohit S Sharma, "A hyperspectral survey of new york city lighting technology," *Sensors*, vol. 16, no. 12, pp. 2047, 2016.
- [14] Ramon Alamús, Salvador Bará, Jordi Corbera, Jaume Escofet, Vicenç Palà, Luca Pipia, and Anna Tardà, "Ground-based hyperspectral analysis of the urban nightscape," *ISPRS Journal of Photogrammetry and Remote Sensing*, vol. 124, pp. 16–26, 2017.
- [15] Gregory Dobler, Federica B Bianco, Mohit S Sharma, Andreas Karpf, Julien Baur, Masoud Ghandehari, Jonathan S Wurtele, and Steven E Koonin, "The urban observatory: a multi-modal imaging platform for the study of dynamics in complex urban systems," *arXiv preprint arXiv:1909.05940*, 2019.
- [16] Michael J Duggin and Dana Piwinski, "Recorded radiance indices for vegetation monitoring using noaa avhrr data; atmospheric and other effects in multitemporal data sets," *Applied optics*, vol. 23, no. 15, pp. 2620–2623, 1984.
- [17] Dominique Courault, Bernard Seguin, and Albert Olioso, "Review to estimate evapotranspiration from remote sensing data: some examples from the simplified relationship to the use of mesoscale atmospheric models," in *ICID workshop on remote sensing of ET for large regions*, 2003, vol. 17, pp. 1–18.
- [18] Bo-Cai Gao, Kathleen B Heidebrecht, and Alexander FH Goetz, "Derivation of scaled surface reflectances from aviris data," *Remote sensing of Environment*, vol. 44, no. 2-3, pp. 165–178, 1993.
- [19] K Staenz, J Secker, B-C Gao, C Davis, and C Nadeau, "Radiative transfer codes applied to hyperspectral data for the retrieval of surface reflectance," *ISPRS Journal of Photogrammetry and Remote Sensing*, vol. 57, no. 3, pp. 194–203, 2002.
- [20] Paul M Mather and Magaly Koch, *Computer processing of remotely-sensed images: an introduction*, John Wiley & Sons, 2011.
- [21] Leonid V Katkovsky, Anton O Martinov, Volha A Siliuk, Dmitry A Ivanov, and Alexander A Kokhanovsky, "Fast atmospheric correction method for hyperspectral data," *Remote Sensing*, vol. 10, no. 11, pp. 1698, 2018.
- [22] AI Hirsch, AM Michalak, LM Bruhwiler, W Peters, EJ Dlugokencky, and PP Tans, "Inverse modeling estimates of the global nitrous oxide surface flux from 1998–2001," *Global Biogeochemical Cycles*, vol. 20, no. 1, 2006.
- [23] Anna M Michalak, Adam Hirsch, Lori Bruhwiler, Kevin R Gurney, Wouter Peters, and Pieter P Tans, "Maximum likelihood estimation of covariance parameters for bayesian atmospheric trace gas surface flux inversions," *Journal of Geophysical Research: Atmospheres*, vol. 110, no. D24, 2005.
- [24] W. K. Hastings, "Monte Carlo sampling methods using Markov chains and their applications," *Biometrika*, vol. 57, no. 1, pp. 97–109, 04 1970.
- [25] Nicholas Metropolis, Arianna W Rosenbluth, Marshall N Rosenbluth, Augusta H Teller, and Edward Teller, "Equation of state calculations by fast computing machines," *The journal of chemical physics*, vol. 21, no. 6, pp. 1087–1092, 1953.
- [26] Federica B Bianco, Steven E Koonin, Charlie Mydlarz, and Mohit S Sharma, "Hypertemporal imaging of nyc grid dynamics: Short paper," in *Proceedings of the 3rd ACM International Conference on Systems for Energy-Efficient Built Environments*, 2016, pp. 61–64.
- [27] Julien Baur, Gregory Dobler, Federica Bianco, Mohit Sharma, and Andreas Karpf, "Persistent hyperspectral observations of the urban lightscape," in *2018 IEEE Global Conference on Signal and Information Processing (GlobalSIP)*. IEEE, 2018, pp. 983–987.
- [28] A Sweeney, RP West, and C O'connor, "Parameters affecting the albedo effect in concrete," *Department of Civil, Structural and Environmental Engineering, Trinity College, Dublin*, vol. 2, pp. 1–8, 2011.
- [29] Yinghong Qin, Yanlin Zhao, Xuejun Chen, Lei Wang, Fanghua Li, and Ting Bao, "Moist curing increases the solar reflectance of concrete," *Construction and Building Materials*, vol. 215, pp. 114–118, 2019.
- [30] Martyna Dominiak-Świgoń, Paweł Olejniczak, Maciej Nowak, and Marlena Lembicz, "Hyperspectral imaging in assessing the condition of plants: strengths and weaknesses," *Biodiversity Research and Conservation*, vol. 55, no. 1, pp. 25–30, 2019.
- [31] FA Kruse, "Comparison of atrem, acorn, and flaash atmospheric corrections using low-altitude aviris data of boulder, co," in *Summaries of 13th JPL Airborne Geoscience Workshop, Jet Propulsion Lab, Pasadena, CA*, 2004.
- [32] Luis Guanter, Rudolf Richter, and Hermann Kaufmann, "On the application of the modtran4 atmospheric radiative transfer code to optical remote sensing," *International Journal of Remote Sensing*, vol. 30, no. 6, pp. 1407–1424, 2009.
- [33] Chris Gueymard, *SMARTS2, a simple model of the atmospheric radiative transfer of sunshine: algorithms and performance assessment*, Florida Solar Energy Center Cocoa, FL, 01 1995.
- [34] Christian A Gueymard, "Parameterized transmittance model for direct beam and circumsolar spectral irradiance," *Solar Energy*, vol. 71, no. 5, pp. 325–346, 2001.
- [35] Christian A Gueymard, "The sun's total and spectral irradiance for solar energy applications and solar radiation models," *Solar energy*, vol. 76, no. 4, pp. 423–453, 2004.
- [36] Eric P Shettle and Robert W Fenn, *Models for the aerosols of the lower atmosphere and the effects of humidity variations on their optical properties*, vol. 79., no. 214, Optical Physics Division, Air Force Geophysics Laboratory, 1979.
- [37] FC Seidel, AA Kokhanowsky, and Michael E Schaepman, "Fast and simple model for atmospheric radiative transfer," *Atmospheric Measurement Techniques*, vol. 3, no. 3, pp. 2225–2273, 2010.
- [38] Daniel Foreman-Mackey, David W Hogg, Dustin Lang, and Jonathan Goodman, "emcee: the mcmc hammer," *Publications of the Astronomical Society of the Pacific*, vol. 125, no. 925, pp. 306, 2013.
- [39] Pearu Peterson, "F2py: a tool for connecting fortran and python programs," *International Journal of Computational Science and Engineering*, vol. 4, no. 4, pp. 296–305, 2009.